

# Optimized noise-resilient surface code teleportation interfaces

Mohamed A. Shalby,<sup>1</sup> Renyu Wang,<sup>1</sup> Denis Sedov,<sup>2</sup> and Leonid P. Pryadko<sup>1</sup>

<sup>1</sup>*Department of Physics and Astronomy, University of California, Riverside 92521 USA*

<sup>2</sup>*Institute for Theoretical Physics III, University of Stuttgart, 70550 Stuttgart Germany*

(Dated: March 10, 2025)

Connecting two surface-code patches may require significantly higher noise at the interface. We show, via circuit-level simulations under a depolarizing noise model with idle errors, that surface codes remain fault tolerant despite substantially elevated interface error rates. Specifically, we compare three strategies—direct noisy links, gate teleportation, and a CAT-state gadget—for both rotated and unrotated surface codes, and demonstrate that careful design can mitigate hook errors in each case so that the full code distance is preserved for both  $X$  and  $Z$ . Although these methods differ in space and time overhead and performance, each offers a viable route to modular surface-code architectures. Our results, obtained with `Stim` and `PyMatching`, confirm that high-noise interfaces can be integrated fault-tolerantly without compromising the code’s essential properties, indicating that fault-tolerant scaling of error-corrected modular devices is within reach with current technology.

**Introduction.** Quantum error correction (QEC) is crucial for achieving large-scale fault-tolerant quantum computation [1]. Surface codes, in particular, offer a compelling balance of high thresholds, planar connectivity, and relative architectural simplicity [2–5].

However, scaling up to large devices poses fabrication, control, and thermal challenges. As a result, there is a growing interest in *modular* quantum processors, where smaller processing modules are interconnected to form a larger, fault-tolerant computing network [6, 7]. A similar approach is also needed in quantum communication to transfer quantum data between different stations at a distance, or in quantum memory to have higher storage capacity [8]. In such systems, the *interfaces* between two modules often exhibit elevated noise compared to the bulk, necessitating special boundary gadgets or coupling strategies to maintain global fault tolerance [9].

Within phenomenological error model, a map to a spin model indicates that a modular quantum computer with modules in the form of sufficiently large square patches of surface code can be below the threshold whenever bulk qubits are, and with any boundary error probability  $q < 1/2$  [10]. More accurate mean-field analysis and circuit-level simulations suggest that error rates for gates across the boundary up to roughly an order of magnitude higher than the threshold required for the bulk operations within each module can be tolerated [9, 10]. This indicates that scalable quantum computing based on modules connected with noisy inter-modular links (whether optical, superconducting, or ion-based) may be feasible with current or near-term technology.

On this front, various technologies are being explored to connect separated quantum modules. For superconducting qubits, waveguide-based couplers [11, 12] or 3D-coaxial cables [13] have shown promise as inter-chip links but can introduce additional loss and decoherence. In photonic architectures, fiber or integrated waveguide channels can mediate entangled links [14–16]. Similarly, trapped-ion platforms use photonic interconnects or phonon-bus couplings [17, 18] to bridge multiple ion traps. Such connectors, whether based on stationary or

flying qubits, may require additional boundary gadgets, e.g., teleportation circuits. An important question is how can such interface gadgets be integrated with the surface code measurement cycle for qubits in the bulk.

The goal of this work is to compare the performance of several interface gadgets under generic circuit noise, with fixed boundary-to-bulk error rate ratios  $\gamma \equiv q/p$ . Specifically, we construct heavily optimized circuits for two such methods, *cat state* (CAT) gadget [19] and *gate teleportation* (GT) gadget [20], as well as a simpler noisy direct-link (DL) interface [Fig. 1], with both *rotated* and *unrotated* surface codes. For all six boundary configurations, using error rate ratios  $\gamma \in \{1, 10\}$ , we calculate (pseudo)thresholds and values of  $\Lambda$  at fixed  $p = 0.345\%$ . We conclude that all these methods can be used to connect patches of surface codes, with reasonably close (pseudo)thresholds and below-threshold behavior. In particular, our results validate approximations made in Ref. [9] for the case of gate teleportation gadgets connecting two unrotated surface code patches.

**Circuits:** In the bulk, we adopt the standard  $\mathcal{N}Z$  surface code measurement schedule [21]. This ensures that weight-two hook errors are aligned across logical operators, thus ensuring that any fault causes no more damage than a single-qubit error should.

For DL gadget, the same schedule is also adopted at the boundary, with the error rate  $q = \gamma p$  for the two-qubit gates crossing the boundary indicated with a red dashed line. Here  $p$  is the error rate in the bulk of both patches, and  $\gamma$  is the boundary-to-bulk error rate ratio. Two-qubit versions of such a single-ancilla measurement circuit, for measuring  $ZZ$  and  $XX$ , are shown in Fig. 1(a), for easier comparison with the other two gadgets.

Circuit diagrams for the CAT and GT gadgets, respectively, are shown in Fig. 1(b) and (c). Again, each gadget is shown in two variants to accommodate either a  $Z$ -type or an  $X$ -type stabilizer generator. For clarity, we focus on coupling only two qubits residing on separate patches. Any CNOT gate crossing this line is treated as a high-noise, long-range operation, thereby introducing elevated error rates at the interface.

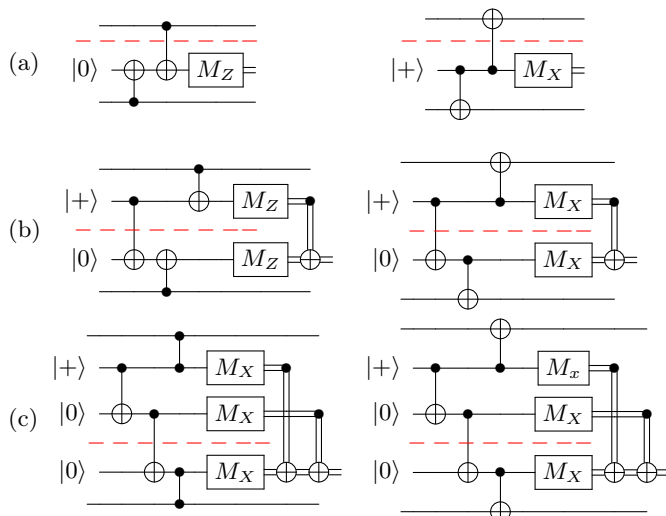


Figure 1. (Color online) (a) DL measurement for two data qubits across the boundary. Left:  $ZZ$  product; Right:  $XX$  product. (b) same for CAT gadget. (c) same for GT gadget. Red dashed lines indicate the interface location.

The same gadgets can couple multiple qubits on both sides as required, depending on the code type, stabilizer weight, measurement schedule, and interface geometry. Also, each of these syndrome-extraction circuits can be remapped into alternate but logically equivalent forms [22]. Such transformations can be particularly advantageous for specific hardware platforms, where gate availability, operation times, or parallelization opportunities may differ significantly.

While DL measurement does not affect the depth of the measurement circuit, CAT and GT gadgets require circuits with 5 CNOT gates applied sequentially (circuit depth 5). To keep these circuits in sync with measurements in the bulk, we insert an additional idle step, thus also increasing the depth of the bulk measurement circuit to 5.

Second challenge in designing circuits for CAT and GT boundary gadgets is to suppress the hook errors. Although partial remedies (e.g., reversal of measurement schedules between rounds [23]) can limit the damage, our focus here is on configurations that maintain the full code distance for both logical observables.

Damaging hook errors appear when a stabilizer generator of weight four is split evenly between patches, effectively creating two pairs of data qubits. In this case, hook errors are oriented along the boundary, necessarily reducing the effective distance with respect to either logical  $X$  or logical  $Z$  observable.

In unrotated surface codes, boundary stabilizer generators typically encompass three data qubits on one side and only one on the other [Fig. 2(a)], and hook errors can be controlled just by choosing the addressing schedules. However, in rotated surface codes, a linear boundary yields a 2–2 split [Fig. 2(b)], prompting us to adopt a zigzag boundary geometry [Fig. 2(c)]. This design en-

sures no stabilizer generator is split evenly between the two patches, eliminating critical hook errors at the interface.

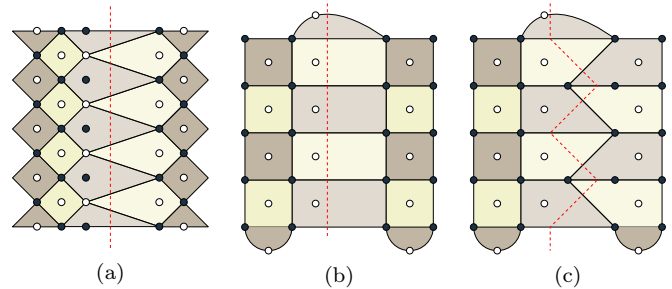


Figure 2. (Color online) Different surface-code interface configurations. Panel (a) shows two patches of unrotated surface code with a straight-line interface, panel (b) depicts a rotated surface code with a straight-line interface, and panel (c) shows a rotated surface code with a zigzag interface.

In Fig. 3, as a representative sample, we show detailed layouts and addressing schedules for two distance-3 interfaces, rotated surface code with CAT gadget at the interface (Left) and unrotated surface code with gate teleportation (Right). The modified boundary design for rotated surface codes effectively avoids critical hook errors. These, as well as all other circuits we designed, can be implemented in a single-layer planar qubit layout.

The addressing schedule is shown in Fig. 3 by the numbers which indicate the time step for addressing a particular data qubit or executing a particular CNOT gate. In the bulk, this is the familiar  $\mathcal{WZ}$  pattern, augmented by an additional initial step that accommodates gadget-specific requirements. During this added step, all other ancillas and data qubits remain idle and thus experience idling noise. This design ensures that circuit modifications at the interface preserve the overall fault tolerance of the system.

**Error model:** We used a standard circuit-level depolarizing noise model with idle errors, subject to four key assumptions. First, single-qubit gate errors occur after every single-qubit operation with probability  $p_1$ . Second, two-qubit gate errors arise after each entangling operation (e.g., CNOT) with probability  $p_2$ . Third, qubits that are not actively involved in an operation are exposed to idling errors, modeled as single-qubit depolarizing noise with probability  $p_{\text{idle}}$ . Finally, initialization and measurement errors occur with probability  $p_{\text{flip}}$ , manifesting as an  $X$ -type error for a  $Z$ -basis measurement (or a  $Z$ -type error for an  $X$ -basis measurement) both immediately after initialization and just before measurement.

In our simulations, we set  $p_1 = p_2 = p_{\text{idle}} = p_{\text{flip}}$ . Within the *bulk* of each surface-code patch, these error probabilities are collectively denoted by  $p$ . By contrast, at the *interface*, the two-qubit gate error rate,  $p_2$ , is elevated by a factor  $\gamma$ , so  $q = \gamma p$ . We primarily focus on the case of  $\gamma = 10$ , which highlights scenarios with significantly higher boundary noise, while  $\gamma = 1$  serves as a

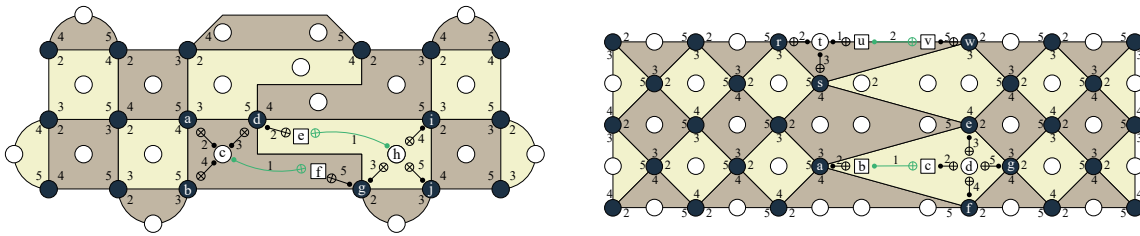


Figure 3. (Color online) Detailed layouts and addressing schedules (numbers) for rotated surface code with CAT gadget at the interface (Left) and unrotated surface code with gate teleportation (Right). Data qubits are represented with dark circles, ancillary qubits with white circles, while extra qubits are represented using white squares. CNOT gates with elevated noise are colored green. More details in the Appendix

baseline to isolate the effects of interface gadgets.

**Simulations:** We simulated the described circuits with `Stim`[24]. Specifically, we implemented interfaces between a pair of square distance- $d$  patches of surface code, for odd distances in the range  $3 \leq d \leq 11$ . Two variants of each simulation were constructed, with data qubits initially prepared in  $|0\rangle$  or  $|+\rangle$  states, and the final data-qubit measurement done in the  $Z$  or  $X$  basis, respectively. Each circuit included initial data qubit preparation,  $N = d$  identical measurement rounds, followed by a final round of data qubit measurements. In addition, one- and two-qubit Pauli errors were inserted at the end of every time step as required by the error model.

The complete `Stim` simulation also includes the annotations for *detector events* representing known relations between measurements in the absence of errors, and the *observables* which are used to check whether the decoding was correct. For example, the detector events could be the differences between measurement results in the subsequent rounds of stabilizer measurements, or similar relations between the  $X$ - or  $Z$ -stabilizer measurements in the last round and the final data-qubit measurements. Similarly, the observables correspond to the  $X$ - or  $Z$ -logical operators whose expected values in the absence of errors can be deduced from the data qubit initialization and the final measurement results.

The constructed circuits were simulated on a laptop computer with `Stim` [24], using `PyMatching` [25] decoder. For each point, the maximum number of samples was set to  $3 \times 10^6$ , with termination after  $3 \times 10^3$  logical errors.

**Simulation results** for each family of circuits (varying by interface gadget, code orientation, and the observable measured) and for each value of the interface noise factor  $\gamma$ , are presented in threshold-style plots, where the logical error rate  $p_L$  is plotted as a function of the error parameter  $p$ , for the odd patch distances  $3 \leq d \leq 11$ . Such plots for the two boundary configurations in Fig. 3 are shown in Figs. 4 and 5. (The complete set of plots is given in the Appendix.)

At smaller values of  $p$ , all curves for codes with distance  $d = 2t + 1$  have the logarithmic slope approximately equal  $t + 1$  (asymptotic form  $\propto p^{t+1}$ ), in agreement with the expected circuit distances (we only were able to explicitly verify the circuit distances for  $d \leq 7$ ).

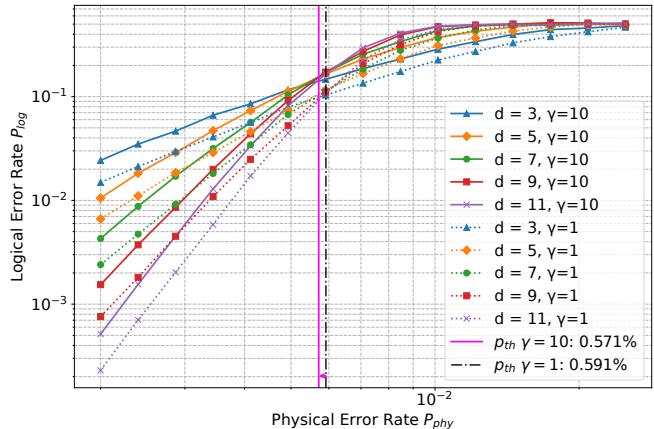


Figure 4. (Color online) Logical error vs. physical error rates for rotated surface code patches connected with CAT gadgets. Solid lines are used for  $\gamma = 10$ , dashed lines for  $\gamma = 1$ . The logical observable being measured is *across* the interface. Vertical lines indicate the positions of the crossing points.

The curves for different distances show reasonably good crossing points, with logical error rates decreasing (increasing) with the distance, respectively, to the left (to the right) of the crossing point. Generally, a threshold is defined as the value of the physical error rate  $p$  at which the logical error rate  $p_L$  stops improving with increasing code distance  $d$ , in the limit of large distances. In a finite-size simulation, an abscissa of a crossing point gives a pseudothreshold, a finite-size approximation to the threshold. The pseudothreshold values  $p_{th}(\gamma)$  computed by fitting the data close to the crossing points are collected in Tab. I.

In addition, in Tab. I we also give the lambda-factors  $\Lambda_{5/7}(\gamma)$ , computed at the fixed physical error rate  $p = 3.45 \times 10^{-3}$  as a ratio of logical error rates for  $d = 5$  and  $d = 7$ . This parameter quantifies how strongly the logical error rate is suppressed with increasing code distance. In general,

$$\Lambda_{d/(d+2)} = p_L^{(d)} / p_L^{(d+2)},$$

so larger  $\Lambda$  values correspond to more effective distance-based error suppression.

Code Type	Gadget	Depth	Parallel				Across			
			$p_{th}(1)$	$p_{th}(10)$	$\Lambda_{5/7}(1)$	$\Lambda_{5/7}(10)$	$p_{th}(1)$	$p_{th}(10)$	$\Lambda_{5/7}(1)$	$\Lambda_{5/7}(10)$
Rotated	DL	4	0.007831	0.007800	6.433	5.873	0.006782	0.006308	1.894	1.630
Rotated	CAT	5	0.006551	0.006494	3.116	3.418	0.005914	0.005714	1.590	1.488
Rotated	GT	5	0.006537	0.006411	3.442	3.503	0.005878	0.005472	1.609	1.411
Unrotated	DL	4	0.007648	0.007676	6.632	6.225	0.007681	0.007317	2.957	2.412
Unrotated	CAT	5	0.006396	0.006276	5.111	4.559	0.006321	0.006026	2.027	1.859
Unrotated	GT	5	0.006649	0.006491	6.778	5.895	0.006145	0.005727	1.946	1.649

Table I. Combined threshold estimates  $p_{th}(\gamma)$  and Lambda factors  $\Lambda(\gamma)$  for different surface-code configurations at boundary noise ratios  $\gamma = 1$  and  $\gamma = 10$ . “Parallel” and “across” refers to orientation of logical observables with respect to the interface.  $\Lambda_{5/7}$  are evaluated at  $p_{phys} = 3.45 \times 10^{-3}$ .

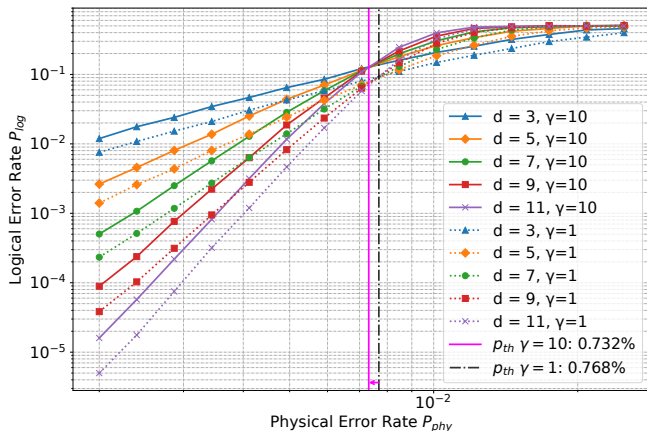


Figure 5. (Color online) Same as in Fig. 4 but for the DL gadget.

It is easily seen from Tab. I that both the threshold error rates and the  $\Lambda$ -values are significantly higher when the observable is measured parallel to (rather than across) the interface. This is not surprising, since these observables detect decoding errors corresponding to conjugate logical operators. That is, an observable *across* the interface shows logical errors (domain walls) *along* the boundary. Likelihood of such an error is higher even for  $\gamma = 1$  because of the chosen geometry; it is further increased for  $\gamma > 1$  because of higher fault probability near the boundary. A quantum code must protect the encoded data from any errors. Thus, in the subsequent discussion we focus on the parameters with the observables oriented across the interface.

It is also seen from Table I that unrotated codes consistently attain higher thresholds, in agreement with much higher entropy of minimal-weight error chains in this configuration, and aligning with well-established findings in surface-code literature. This advantage does come with increased qubit overhead, since unrotated patches require more data qubits to reach a given code distance.

Unlike for a DL interface, use of CAT and GT gadgets forces an increase of the bulk measurement circuit depth by 25%, and one would expect a comparable decrease

of the (pseudo)thresholds with respect to DL interface. In reality, at  $\gamma = 10$ , the decrease is about 13% for rotated surface codes, and close to 18% for regular. We believe this to be an entropic effect. Namely, with a rotated surface code, multiple errors on the boundary force minimal-weight error chains to stay close to the interface, thus reducing the entropy and compensating, to a degree, the threshold reduction. In contrast, minimal-weight error chains are linear for regular surface codes, and their entropy is not expected to change as much.

**In conclusion**, we performed a careful comparison of three boundary-connection strategies—DL interface, CAT gadget, and GT gadget—both for rotated and unrotated surface codes under circuit-level depolarizing noise. Our simulations demonstrate that all three methods maintain fault tolerance even with a significantly elevated noise at the interface.

DL requires the least resources, adding no ancillary qubits and no circuit depth beyond standard surface-code measurement cycle. Respectively, for both rotated and unrotated surface codes, DL exhibits smallest logical error rates and highest thresholds, which is not surprising given the absence of additional idling noise. CAT and GT gadgets, in contrast, require additional ancillary qubits and an increase of circuit depth by one CNOT gate. Nevertheless, both methods achieve robust error suppression, with the thresholds down from DL interface values by less than 20%. While the thresholds and the  $\Lambda$ -factors are consistently smallest for rotated surface codes, the relative decrease of thresholds and  $\Lambda(10)$  from those for DL interface are both under 10%.

These results emphasize that boundary gadgets, verified here in circuit-level quantum memory simulations, can also serve as a basis for more dynamic approaches, such as lattice surgery in modular quantum architectures. Designers must weigh qubit availability, specialized hardware constraints, gate availability, and error-model considerations when selecting an interface strategy. Techniques like hardware-tailored scheduling, biased-noise optimization, or partial measurement schemes may further enhance error suppression without incurring excessive ancillary costs. Overall, our study confirms that thoughtfully engineered boundary connections can preserve fault



tolerance in modular surface-code architectures despite considerably higher interface noise.

**Acknowledgments:** This work was supported in part by the NSF Division of Physics via the grant 2112848.

- 
- [1] P. W. Shor, Fault-tolerant quantum computation, in *Proc. 37th Ann. Symp. on Fundamentals of Comp. Sci.*, IEEE (IEEE Comp. Soc. Press, Los Alamitos, 1996) pp. 56–65, [quant-ph/9605011](#).
- [2] A. Y. Kitaev, Fault-tolerant quantum computation by anyons, *Ann. Phys.* **303**, 2 (2003).
- [3] E. Dennis, A. Kitaev, A. Landahl, and J. Preskill, Topological quantum memory, *J. Math. Phys.* **43**, 4452 (2002).
- [4] A. G. Fowler, M. Mariantoni, J. M. Martinis, and A. N. Cleland, Surface codes: Towards practical large-scale quantum computation, *Phys. Rev. A* **86**, 032324 (2012).
- [5] S. B. Bravyi and A. Y. Kitaev, Quantum codes on a lattice with boundary, [quant-ph/9811052](#) (1998), unpublished.
- [6] C. Monroe, R. Raussendorf, A. Ruthven, K. R. Brown, P. Maunz, L.-M. Duan, and J. Kim, Large-scale modular quantum-computer architecture with atomic memory and photonic interconnects, *Phys. Rev. A* **89**, 022317 (2014).
- [7] N. Nickerson, J. F. Fitzsimons, and S. C. Benjamin, Freely scalable quantum technologies using cells of 5-to-50 qubits with local networking, *Physical Review X* **4**, 041041 (2014).
- [8] S. Muralidharan *et al.*, Optimal architectures for long distance quantum communication, *Scientific Reports* **6**, 20463 (2016).
- [9] J. Ramette, J. Sinclair, N. P. Breuckmann, and V. Vuletić, Fault-tolerant connection of error-corrected qubits with noisy links, [arXiv:2302.01296 \[quant-ph\]](#) (2023), unpublished.
- [10] D. Sedov, R. Wang, and L. P. Pryadko, [Surface code error correction in a modular quantum computer](#), APS March Meeting presentation T73.00014 (2023), [unpublished].
- [11] P. Magnard, A. Kurpiers, T. Walter, *et al.*, Microwave quantum link between superconducting circuits housed in spatially separated cryogenic systems, *Physical Review Letters* **125**, 260502 (2020).
- [12] P. Campagne-Ibarcq, A. Eickbusch, S. Touzard, *et al.*, Quantum error correction of a qubit encoded in grid states of an oscillator, *Nature* **584**, 368 (2020).
- [13] D. Rosenberg, D. Kim, A. Y. M. Chen, *et al.*, 3D integrated superconducting qubits, *npj Quantum Informa-*  
*tion* **3**, 42 (2020).
- [14] D. Main, P. Drmota, D. P. Nadlinger, E. M. Ainley, A. Agrawal, B. C. Nichol, R. Srinivas, G. Araneda, and D. M. Lucas, Distributed quantum computing across an optical network link, *Nature* **638**, 383 (2025).
- [15] J. S. Pelc, C. R. Phillips, Q. Zhang, *et al.*, Frequency conversion of single photons in a solid-state emitters–quantum dot platform, *Optics Express* **19**, 21445 (2011).
- [16] M. Li, S. Chen, X. Ding, *et al.*, Recent advances in integrated quantum photonics, *Advanced Quantum Technologies* **5**, 2100111 (2022).
- [17] C. Monroe, W. C. Campbell, L.-M. Duan, Z.-X. Gong, A. V. Gorshkov, P. W. Hess, R. Islam, K. Kim, N. M. Linke, G. Pagano, P. Richerme, C. Senko, and N. Y. Yao, Programmable quantum simulations of spin systems with trapped ions, *Rev. Mod. Phys.* **93**, 025001 (2021).
- [18] L. J. Stephenson, S. M. Clark, L. Bryant, *et al.*, High-rate, high-fidelity entanglement of qubits across an elementary quantum network, *Physical Review Letters* **124**, 110501 (2020).
- [19] S. Huang and K. R. Brown, Between shor and steane: A unifying construction for measuring error syndromes, *Phys. Rev. Lett.* **127**, 090505 (2021).
- [20] D. Gottesman and I. L. Chuang, Quantum teleportation is a universal computational primitive, *Nature* **402**, 390 (1999).
- [21] Y. Tomita and K. M. Svore, Low-distance surface codes under realistic quantum noise, *Phys. Rev. A* **90**, 062320 (2014), [1404.3747](#).
- [22] A. Barenco, C. H. Bennett, R. Cleve, D. P. DiVincenzo, N. Margolus, P. Shor, T. Sleator, J. A. Smolin, and H. Weinfurter, Elementary gates for quantum computation, *Phys. Rev. A* **52**, 3457 (1995).
- [23] D. M. Debroy, M. McEwen, C. Gidney, N. Shutty, and A. Zalcman, Luci in the surface code with dropouts (2024).
- [24] C. Gidney, Stim: a fast stabilizer circuit simulator, *Quantum* **5**, 497 (2021).
- [25] O. Higgott, PyMatching: a Python package for decoding quantum codes with minimum-weight perfect matching, [arXiv:2105.13082](#) (2021), unpublished.

## APPENDIX

Here we give additional details about the constructed circuits and the threshold-style plots for all interface geometries. Namely, Figs. 6 and 7, give layouts, addressing schedules, and full boundary-gadget circuits, respectively, for rotated surface code patches with CAT gadgets, and unrotated surface code patches with GT gadgets. Fig. 8 shows the complete set of threshold-style plots grouped by surface code type (rotated or unrotated), logical observable direction (*across* or *parallel*), and gadget type [CAT, GT, and DL]. Each plot shows curves for odd distances in the range  $3 \leq d \leq 11$  and for boundary noise factors  $\gamma \in \{1, 10\}$ .

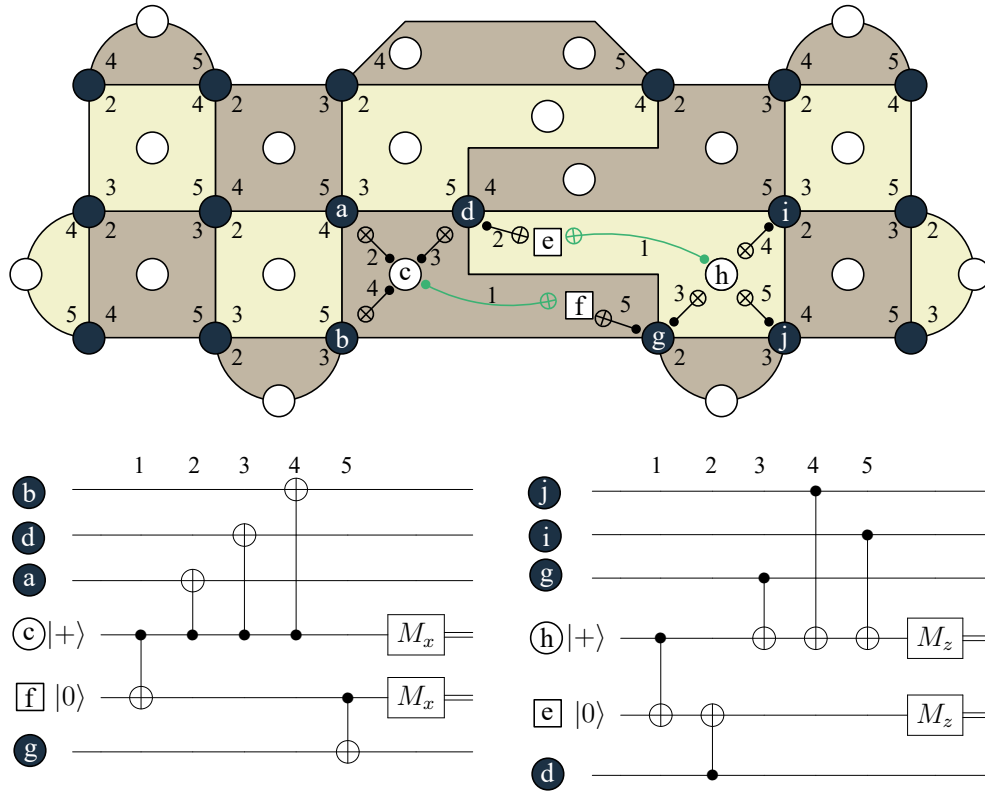


Figure 6. Layout with schedule and circuit for two patches of rotated surface code  $d=3$  connecting using CAT. Data qubits are dark circles, while ancillas are white circles, the squares denotes the added ancillas for CAT. Green CNOT gates have elevated noise.

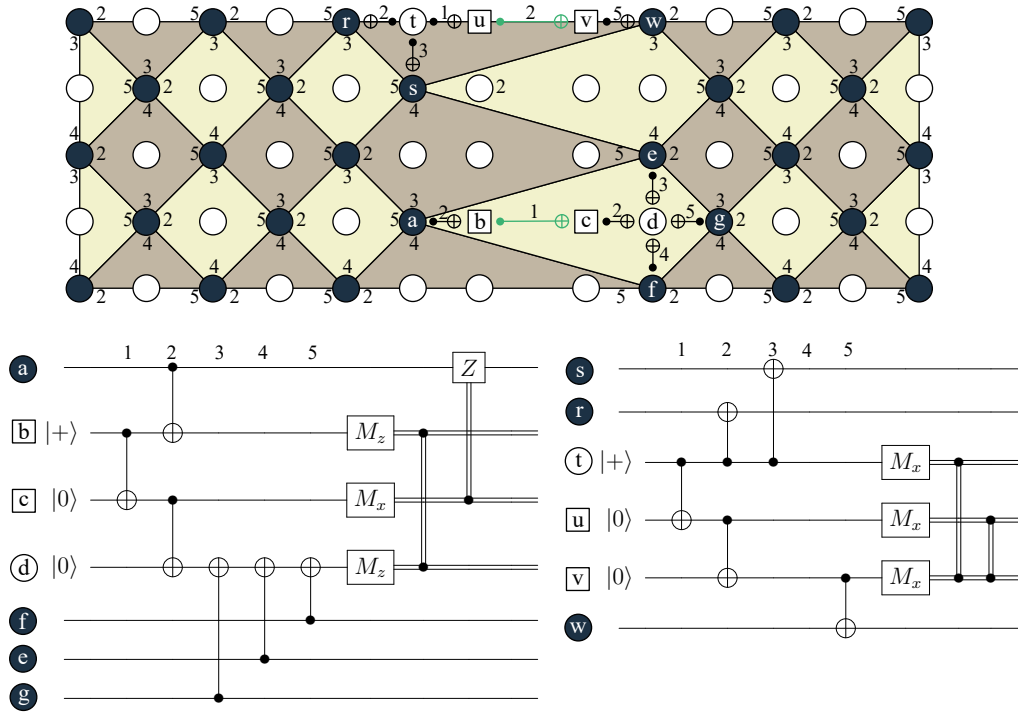


Figure 7. Layout with schedule and circuit for two patches of unrotated surface code  $d=3$  connected using GT. Data qubits are dark circles, while ancillas are white circles, the squares denotes the added ancillas for GT. Green CNOT gates have elevated noise.

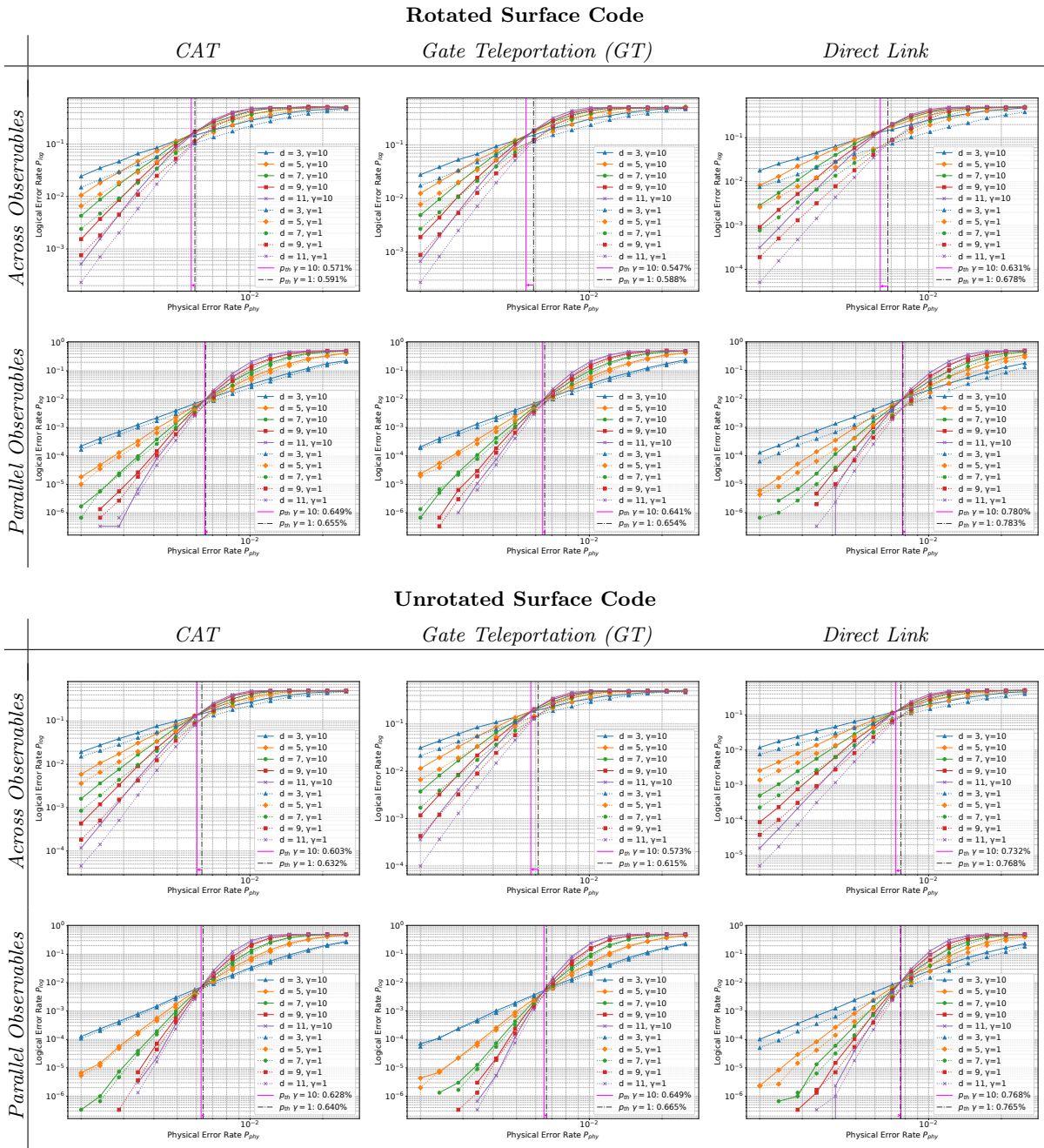


Figure 8. Comparison of rotated (top) and unrotated (bottom) surface-code configurations at  $\gamma = 1$  and  $\gamma = 10$ . Each row corresponds to logical observables *across* or *parallel* to the interface, while each column shows results for a different boundary gadget (CAT, GT, or Direct Link).